Feature Article:

DOI. No. 10.1109/MAES.2024.3432105

LEO Satellite Orbit Prediction via Closed-Loop Machine Learning With Application to Opportunistic Navigation

Zaher M. Kassas and Samer Hayek, **The Ohio State University, Columbus, OH 43210 USA**

Jamil-Haidar Ahmad, **University of California, Irvine, CA 92697 USA**

INTRODUCTION

Over the past few decades, the ambitious glorified image of Earth connected through a web weaved from low Earth orbit (LEO) satellites has taken the world by storm, promising high-resolution remote sensing images, space-based optical mesh networks, and global, high-availability, high-bandwidth, and low latency Internet [1]. While some early LEO companies, such as Iridium, Intermediate Circular Orbit, and Teledesic, made haste in securing their position in this space race, they suffered financial setbacks, and the reliability and viability of LEO constellations were scrutinized and experienced skepticism. However, the past few years witnessed notable strides in small satellite technology [2] and ground-breaking developments in launch reduction costs [3]. With the demand for LEO satellites at an all-time high, due to their potential for enabling new communication technologies (e.g., 6G nonterrestrial networks and beyond) [4], revolutionizing passive sensing [5], and refashioning positioning, navigation, and timing (PNT) [6], the space race is back on. Major technology giants, such as SpaceX, Amazon, and Boeing, as well as government agencies are rushing to launch tens of thousands of satellites for communication, Internet connectivity, and geographical sensing purposes [7]. With the dawn of LEO megaconstellations, tracking these space objects to a high degree of accuracy is evermore important [8]. Aside from "classic" space situational awareness purposes, improved LEO ephemerides enables the exploitation of LEO satellite signals of opportunity for PNT purposes [9].

Opportunistic PNT with "noncooperative" LEO satellites [10] brings upon the following challenges of:

i) extracting navigation observables (pseudorange, carrier phase, and/or Doppler) from the satellites' partially known or unknown signals;

ii) compensating for the satellites' unknown synchronization and timing errors;

iii) estimating the satellites' unknown ephemerides.

To address the first challenge of signal exploitation, several receivers have been proposed to extract navigation observables from partially known signals [11], [12], [13], [14]. For unknown LEO signals, the paradigm of cognitive opportunistic navigation has shown tremendous promise in blindly acquiring and tracking several "noncooperative" LEO constellations: Starlink, OneWeb, Orbcomm, Iridium, and National Oceanic and Atmospheric Administration [15], [16], [17], [18], [19]. Several recent studies have offered solutions for dealing with the second challenge of synchronization [20], [21], [22]. This article addresses the third challenge of ephemerides estimation.

The best publicly available estimate for a LEO satellite's ephemeris is given at the initial time provided by two-line element (TLE) files published by North American Aerospace Defense (NORAD), which would then be propagated through a propagator [e.g., simplified general perturbations 4 (SGP4)]. However, the initial ephemeris could be off by a few kilometers, and as the satellite's ephemeris gets propagated through time, the error continues to increase, only to be corrected when a new TLE file

Authors' current address: Zaher M. Kassas and Samer Hayek are with the Department of Electrical and Computer Engineering, The Ohio State University, Columbus, OH 43210 USA (e-mail: zkassas@ieee.org, watchihayek.1@osu.edu). Jamil Haidar-Ahmad was with the Department of Electrical Engineering and Computer Science, University of California, Irvine, CA 92697 USA (e-mail: jhaidara@uci.edu). *(Corresponding author: Zaher M. Kassas.)*

Manuscript received 9 January 2024, revised 25 June 2024; accepted 4 July 2024, and ready for publication 2 August 2024.

Review handled by Daniel O'Hagan.

0885-8985/24/$26.00 © 2024 IEEE

Image licensed by Ingram Publishing

is published the next day. The daily update limits the use of LEO signals of opportunity for PNT, since such large ephemeris error translates to unacceptably large positioning error [9].

Several analytical and numerical satellite orbit determination algorithms have been developed to propagate satellites' states as well as associated uncertainty [23]. These propagators take into consideration, to various extents, multiple sources of perturbing forces, e.g., Earth's nonuniform gravitational field, atmospheric drag, solar radiation pressure, and third-body attraction (e.g., Sun and Moon) [24]. The SGP4 [25] analytical propagator is used to generate ephemerides from a set of mean orbital elements given at a reference epoch in TLE files, which are published and updated periodically by the NORAD [26]. However, analytical orbit determination methods are based on limited dynamical models and mean elements, resulting in ephemerides that may not meet PNT accuracy requirements [27], [28]. Space agencies usually employ high-precision orbit propagators (HPOP), which are numerical propagators used in conjunction with precise force models. However, numerical propagators require large amounts of data and significant computation time, rendering them undesirable for real-time PNT purposes; in addition to requiring specific knowledge about the satellites (e.g., area, mass, etc.) and space environment, which may not be publicly available.

Machine learning (ML) has shown tremendous potential in radar and communications [29], and its powerful modeling capabilities have been recently studied to provide a less parameter-reliant orbit propagation solution [30], [31]. In [32] and [33], distribution regression was used for orbit determination of objects in LEO. Propagating LEO satellite orbits was studied in [34] and [35] via neural networks (NNs), support vector machines (SVMs), and Gaussian processes (GPs). A simulation study developed in [36] showed that NNs possess high regression capabilities compared with SVMs and GPs. Several NN architectures, such as time-delay NN (TDNN) and long short-term memory (LSTM) NNs, were studied in [37].

For orbit determination, an ML model would be given the task of utilizing data relevant to a LEO satellite's ephemeris as inputs and using this information to predict the satellite's future ephemeris; hence, supervised learning. Unlike deep learning models, where the feature extraction step of the process is automated, enabling the use of large datasets, classical ML requires researchers to determine the set of features, which would allow a model to understand the differences between structured data inputs. This article focuses on a classical ML approach, since large amounts of reliable and highly accurate LEO satellite ephemerides are not available. Furthermore, a large and complex deep learning model would take significantly increased time for both training and inference, rendering it difficult to apply in real-time applications. To achieve a computationally feasible ML solution for orbit propagation, this article utilizes the power of the widely used analytical propagator, SGP4, and proceeds to correct its errors.

Applying NN for improving the LEO orbit prediction with application to opportunistic navigation has been studied recently. In [38], a TDNN was trained on the LEO satellite's position, produced by a Global Navigation Satellite System (GNSS) receiver onboard the LEO satellite, which is broadcast in the LEO satellite's downlink signal. Experimental results demonstrated the efficacy of the TDNN by showing improved ground vehicle navigation with two Orbcomm LEO satellites whose ephemerides are predicted with the NN. In [39], TDNN and LSTM NN architectures were compared, and it was concluded that the TDNN's accuracy was higher. The NN training utilized HPOP [40], which was properly initialized using Orbcomm LEO satellite's position, produced by LEO's onboard GNSS receiver, and decoded from the first received measurement epoch. It was demonstrated that the NN was capable of estimating the position of the satellite to meter-level accuracy over a short time period. In [41],

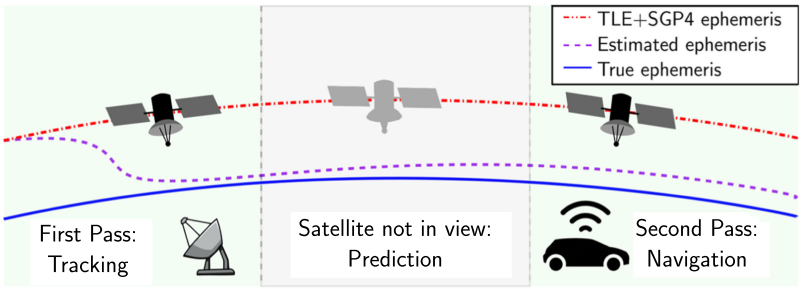

Figure 1.
Proposed framework. (i) *LEO satellite first pass:* A terrestrial receiver with knowledge of its position tracks the LEO satellite. The LEO satellite's states are initialized with SGP4-propagated TLE data, and are subsequently estimated via an EKF during the period of satellite visibility, utilizing the carrier phase measurements. (ii) *LEO satellite not in view:* an NN is trained on the estimated ephemeris and is used to propagate the LEO satellite orbit for the period where the satellite is not in view. (iii) *LEO satellite second pass:* a terrestrial receiver with *no* knowledge of its position uses the ML-predicted LEO ephemeris along with its carrier phase measurements from received LEO signals to estimate its own position via an EKF.

two types of architectures were compared: (i) a TDNN whose time delay aspect is the NN's outputs being fed back as delayed inputs, and (ii) a nonlinear autoregressive with exogenous inputs (NARX), which takes SGP4-propagated position states as exogenous inputs. It was concluded that the NARX architecture offered the best orbit propagation accuracy, which was demonstrated in improved localization of a stationary receiver with signals from a single LEO Orbcomm satellite with NN-predicted ephemeris. It was also concluded that to obtain the improved ephemeris, the NN would only need to output a weighted version of a time-shifted SGP4-propagated ephemeris. Therefore, one method for ephemeris propagation when given a sparse amount of data relating to a satellite's true position is to find a time shift that matches the SGP4-propagated ephemeris with the satellite's true ephemeris and use that time-shifted ephemeris. This conclusion was corroborated analytically and numerically in a "non-ML-based" fashion in [42].

This article builds on the promising results in [39] and [41] by (i) alleviating the need to train the NN via HPOP, initialized from the GNSS-produced LEO position obtained from the first measurement epoch and (ii) demonstrating the efficacy of a NARX NN in predicting LEO ephemerides by showing improved navigation accuracy of a ground vehicle navigating for 4.05 km with two Orbcomm LEO satellites to an unprecedented level of accuracy.

This article develops the following three-stage framework, termed LEO-NNPON (LEO with NN prediction for opportunistic navigation):

i) tracking during the LEO satellites' first pass;

ii) NN-based prediction while the LEO satellites are not in view;

iii) navigation during the LEO satellites' second pass.

Experimental results of a ground vehicle equipped with an industrial-grade inertial measurement unit (IMU) navigating for 4.05 km with signals from two Orbcomm satellites are presented. Three vehicle navigation frameworks are compared, all initialized with a GNSS-inertial navigation system (INS) position and velocity solution: (i) unaided INS, (ii) LEO-aided INS, which uses SGP4-propagated LEO ephemerides, and (iii) LEO-aided INS, which uses the NN-predicted LEO ephemerides. The three-dimensional (3D) position root-mean-squared error (RMSE) of the unaided INS was 1,865 m, whereas of the LEO-aided INS with SGP4 was 175.5 m. In contrast, the LEO-aided INS with NN was 18.3 m, which is indicative of improved LEO ephemerides.

The rest of this article is organized as follows. The "Problem Description" section overviews the considered problem, outlining the three stages of the proposed framework. The "Model Description" section describes the different models involved in the framework: LEO satellite dynamics, clock error dynamics, navigator kinematics, and LEO measurement model. The " LEO-NNPON Framework: Tracking, Prediction, and Navigation" section details the proposed framework stages: tracking, prediction, and navigation. The "Experimental Results" section gives the experimental results. Finally, the "Conclusion" section concludes this article.

PROBLEM DESCRIPTION

This article considers the problem of enhancing LEO satellite orbit prediction via a closed-loop trained NN. The accuracy of the NN predicted ephemeris is demonstrated in the application of ground-based opportunistic navigation with LEO signals, whereby the trajectory of a ground-based vehicle is estimated to a higher degree of accuracy when utilizing the NN predicted ephemeris, as compared to when utilizing SGP4-predicted ephemeris. The considered problem, depicted in Figure 1, is composed of the following three stages:

1) *First pass (tracking):* A LEO satellite with poorly known ephemeris (e.g., initialized from TLE files and propagated via SGP4 until the time the satellite is in view) flies overhead a ground-based tracker, which has knowledge of its own position (e.g., from GNSS). While overhead, the tracker-mounted receiver listens to the LEO satellite's downlink signals, extracting measurements (pseudorange, carrier phase, and/or Doppler). These measurements are fused via a nonlinear filter [e.g., extended Kalman filter (EKF)] to estimate the LEO satellite's states (position and velocity) along with the difference between the LEO satellite's and tracker's clock errors (bias and drift).
2) *Satellite not in view (prediction):* The estimated ephemeris from the first pass is used to train an NN. Once the satellite is no longer in view, the NN is used to predict the satellite's ephemeris.
3) *Second pass (navigation):* The satellite flies over a ground-based navigator (e.g., vehicle), which uses the LEO satellite's downlink signals to navigate as follows. The vehicle-mounted receiver extracts navigation observables (pseudorange, carrier phase, and/or Doppler) from the LEO satellite's downlink signals. These observables are used to aid the vehicle-mounted IMU in a tightly coupled fashion (e.g., via an EKF). The LEO satellite states are obtained from the NN predicted ephemeris.

MODEL DESCRIPTION

This section describes the models governing the proposed LEO-NNPON framework: LEO satellite dynamics model, clock error dynamics model, navigator kinematics model, and LEO measurement model.

LEO SATELLITE DYNAMICS MODEL

The LEO satellite dynamics will be modeled in the Earth-centered inertial (ECI) reference frame, according to the two-body model, including the most significant nonzero mean perturbing acceleration, which corresponds to J_2 effects [23], [43]. The two-body model offers a tradeoff between accurate open-loop prediction, while maintaining a simple analytical Jacobian for estimation error covariance propagation [44], and is given as

$$\ddot{\boldsymbol{r}}_{\text{leo}} = \boldsymbol{a}_{\text{grav}_{J_2}} + \tilde{\boldsymbol{w}}_{\text{leo}}, \qquad \boldsymbol{a}_{\text{grav}_{J_2}} = \frac{dU_{J_2}}{d\boldsymbol{r}_{\text{leo}}} \tag{1}$$

where $\boldsymbol{r}_{\text{leo}} \triangleq [x_{\text{leo}}, y_{\text{leo}}, z_{\text{leo}}]^{\mathsf{T}}$ is the 3D position vector of the LEO satellite in the ECI frame, $\boldsymbol{a}_{\text{grav}_{J_2}}$ is the acceleration due to Earth's nonuniform gravity, including J_2 effects, U_{J_2} is the nonuniform gravity potential of Earth, including J_2 effects at the satellite, and $\tilde{\boldsymbol{w}}_{\text{leo}}$ is a process noise vector with power spectral density (PSD) $\tilde{\mathbf{Q}}_{\text{leo}}$, which attempts to capture the overall acceleration perturbations, including the unmodeled nonuniformity of Earth's gravitational field, atmospheric drag, solar radiation pressure, third-body gravitational forces (e.g., gravity of the Sun and the Moon), and general relativity [24].

The components of $\boldsymbol{a}_{\text{grav}_{J_2}} = [\ddot{x}_{\text{grav}}, \ddot{y}_{\text{grav}}, \ddot{z}_{\text{grav}}]^{\mathsf{T}}$ are

$$\begin{aligned}
\ddot{x}_{\text{grav}} &= -\frac{\mu x_{\text{leo}}}{\|\boldsymbol{r}_{\text{leo}}\|^3}\left[1 + J_2\frac{3}{2}\left(\frac{R_E}{\|\boldsymbol{r}_{\text{leo}}\|}\right)^2\left(1 - 5\frac{z_{\text{leo}}^2}{\|\boldsymbol{r}_{\text{leo}}\|^2}\right)\right] \\
\ddot{y}_{\text{grav}} &= -\frac{\mu y_{\text{leo}}}{\|\boldsymbol{r}_{\text{leo}}\|^3}\left[1 + J_2\frac{3}{2}\left(\frac{R_E}{\|\boldsymbol{r}_{\text{leo}}\|}\right)^2\left(1 - 5\frac{z_{\text{leo}}^2}{\|\boldsymbol{r}_{\text{leo}}\|^2}\right)\right] \\
\ddot{z}_{\text{grav}} &= -\frac{\mu z_{\text{leo}}}{\|\boldsymbol{r}_{\text{leo}}\|^3}\left[1 + J_2\frac{3}{2}\left(\frac{R_E}{\|\boldsymbol{r}_{\text{leo}}\|}\right)^2\left(3 - 5\frac{z_{\text{leo}}^2}{\|\boldsymbol{r}_{\text{leo}}\|^2}\right)\right]
\end{aligned} \tag{2}$$

where μ is Earth's standard gravitational parameter and R_E is the mean radius of the Earth.

CLOCK ERROR DYNAMICS MODEL

The receiver's and LEO satellites' clock error state dynamics are assumed to evolve according to the standard two-state model (namely, a double integrator driven by process noise) [45], whose discrete-time equivalent representation is given by

$$\begin{aligned}
\boldsymbol{x}_{\text{clk},i}(k+1) &= \mathbf{F}_{\text{clk}}\,\boldsymbol{x}_{\text{clk},i}(k) + \boldsymbol{w}_{\text{clk},i}(k) \\
\boldsymbol{x}_{\text{clk},i} &\triangleq \left[c\delta t_i,\, c\dot{\delta} t_i\right]^{\mathsf{T}}, \quad \mathbf{F}_{\text{clk}} = \begin{bmatrix} 1 & T \\ 0 & 1 \end{bmatrix}
\end{aligned} \tag{3}$$

where $i = \{\text{r}, \text{leo}\}$, δt_i is the clock bias, $\dot{\delta} t_i$ is the clock drift, c is the speed of light, T is the constant sampling interval, and $\boldsymbol{w}_{\text{clk},i}$ is the process noise, which is modeled as a discrete-time white noise sequence with covariance

$$\mathbf{Q}_{\text{clk},i} = c^2 \cdot \begin{bmatrix} S_{\tilde{w}_{\delta t,i}} T + S_{\tilde{w}_{\dot{\delta} t,i}} \frac{T^3}{3} & S_{\tilde{w}_{\dot{\delta} t,i}} \frac{T^2}{2} \\ S_{\tilde{w}_{\dot{\delta} t,i}} \frac{T^2}{2} & S_{\tilde{w}_{\dot{\delta} t,i}} T \end{bmatrix} \tag{4}$$

The terms $S_{\tilde{w}_{\delta t,i}}$ and $S_{\tilde{w}_{\dot{\delta} t,i}}$ are the clock bias and drift process noise PSDs, respectively, of the continuous-time counterpart model; which can be related to the power-law coefficients $\{h_{\alpha_i}\}_{\alpha_i=-2}^{2}$, which have been shown through laboratory experiments to characterize the PSD of the fractional frequency deviation of an oscillator from nominal frequency according to $S_{\tilde{w}_{\delta t_i}} \approx \frac{h_{0,i}}{2}$ and $S_{\tilde{w}_{\dot{\delta} t_i}} \approx 2\pi^2 h_{-2,i}$ [45]. The receiver's and LEO satellites' process noise covariances $\mathbf{Q}_{\text{clk}_{\text{r}}}$ and $\mathbf{Q}_{\text{clk}_{\text{leo}}}$ are calculated from (4) using the PSDs associated with the receiver's and LEO satellites' oscillator quality, respectively.

The dynamics of the difference between the receiver's and LEO satellites' clock error states is given by

$$\Delta \boldsymbol{x}_{\text{clk}}(k+1) = \mathbf{F}_{\text{clk}} \Delta \boldsymbol{x}_{\text{clk}}(k) + \Delta \boldsymbol{w}_{\text{clk}}(k) \tag{5}$$

$$\Delta \boldsymbol{x}_{\text{clk}} \triangleq \left[c\Delta\delta t_{\text{r,leo}}, c\Delta\dot{\delta} t_{\text{r,leo}}\right]^{\mathsf{T}}$$

$$c\Delta\delta t_{\text{r,leo}} \triangleq c \cdot [\delta t_{\text{r}} - \delta t_{\text{leo}}], \quad c\Delta\dot{\delta} t_{\text{r,leo}} \triangleq c \cdot \left[\dot{\delta} t_{\text{r}} - \dot{\delta} t_{\text{leo}}\right]$$

where $\Delta \boldsymbol{w}_{\text{clk}}$ is the process noise vector, which has a covariance $\mathbf{Q}_{\Delta\text{clk}}$ given by $\mathbf{Q}_{\Delta\text{clk}} = \mathbf{Q}_{\text{clk}_{\text{r}}} + \mathbf{Q}_{\text{clk}_{\text{leo}}}$.

NAVIGATOR KINEMATICS

The navigator's orientation, position, and velocity are modeled to evolve in time according to the standard strapdown INS kinematic equations, driven by ${}^{b}\boldsymbol{\omega}_{b}$, a 3D rotation rate vector of the body frame $\{b\}$ expressed in $\{b\}$, and ${}^{g}\boldsymbol{a}_{b}$, a 3D acceleration vector of the body in the global frame $\{g\}$ [46]. The vehicle's 3D orientation vector of $\{b\}$ with respect to $\{g\}$, denoted $\boldsymbol{\theta}_{b}$, and 3D position $\boldsymbol{r}_{b}$ expressed in $\{g\}$ are related to the true 3D rotation rate vector ${}^{b}\boldsymbol{\omega}_{b}$ and 3D acceleration vector ${}^{g}\boldsymbol{a}_{b}$ through the following kinematic differential equations:

$$\dot{\boldsymbol{\theta}}_{b}(t) = {}^{b}\boldsymbol{\omega}_{b}(t) \tag{6}$$

$$\ddot{\boldsymbol{r}}_{b}(t) = {}^{g}\boldsymbol{a}_{b}(t). \tag{7}$$

The navigator-mounted IMU contains a triad-gyroscope and triad-accelerometer and produces angular rate $\boldsymbol{\omega}_{\text{imu}}$ and specific force $\boldsymbol{a}_{\text{imu}}$ measurements, which are modeled as

$$\boldsymbol{\omega}_{\text{imu}}(k) = {}^{b}\boldsymbol{\omega}_{b}(k) + \boldsymbol{b}_{\text{g}}(k) + \boldsymbol{n}_{\text{g}}(k) \tag{8}$$

$$\boldsymbol{a}_{\text{imu}}(k) = \mathbf{R}_{g}^{b}(k)[{}^{g}\boldsymbol{a}_{b}(k) - {}^{g}\boldsymbol{g}(k)] + \boldsymbol{b}_{\text{a}}(k) + \boldsymbol{n}_{\text{a}}(k), \quad k = 1, 2, \ldots \tag{9}$$

where $\mathbf{R}_{g}^{b}(k)$ is the rotation matrix from $\{g\}$ to $\{b\}$; ${}^{g}\boldsymbol{g}$ is the acceleration due to gravity in $\{g\}$; $\boldsymbol{b}_{\text{g}}$ and $\boldsymbol{b}_{\text{a}}$ are the gyroscope and accelerometer biases, respectively; and $\boldsymbol{n}_{\text{g}}$ and $\boldsymbol{n}_{\text{a}}$ are measurement noise vectors, which are modeled as white noise sequences with covariances $\mathbf{Q}_{\text{ng}}$ and $\mathbf{Q}_{\text{na}}$, respectively.

The gyroscope and accelerometer biases are assumed to evolve according to velocity random walk dynamics, namely

$$\boldsymbol{b}_{\text{g}}(k+1) = \boldsymbol{b}_{\text{g}}(k) + \boldsymbol{w}_{\text{bg}}(k) \tag{10}$$

$$\boldsymbol{b}_{\text{a}}(k+1) = \boldsymbol{b}_{\text{a}}(k) + \boldsymbol{w}_{\text{ba}}(k) \tag{11}$$

where $\boldsymbol{w}_{\text{bg}}$ and $\boldsymbol{w}_{\text{ba}}$ are bias instability process noise vectors, which are modeled as a discrete-time white noise sequences with covariances $\mathbf{Q}_{\text{bg}}$ and $\mathbf{Q}_{\text{ba}}$, respectively.

MEASUREMENT MODEL

A LEO receiver extracts continuous-time carrier phase measurements from LEO satellites' downlink signals by integrating the Doppler measurement over time [47]. The carrier phase measurement (expressed in meters) made by the receiver on the LEO satellite at time-step k, which represents discrete-time instant $t_k = kT + t_0$ for an initial time t_0, can be modeled in discrete-time as [10]

$$\phi(k) = \|\boldsymbol{r}_{\text{r}}(k) - \boldsymbol{r}_{\text{leo}}(k')\|_{2} + c\left[\delta t_{\text{r}}(k) - \delta t_{\text{leo}}(k'_{l})\right] + \lambda N + c\delta t_{\text{iono}}(k) + c\delta t_{\text{tropo}}(k) + v(k), \quad k = 1, 2, \ldots \tag{12}$$

where k' represents discrete-time at $t_{k'} = kT + t_0 - \delta t_{\text{TOF}}$, with δt_{TOF} being the true time-of-flight (TOF) of the signal from the LEO satellite to the receiver; c is the speed-of-light; $\boldsymbol{r}_{\text{r}}$ and $\boldsymbol{r}_{\text{leo}}$ are the receiver's and LEO satellite's 3D position vectors expressed in the same reference frame; δt_{r} and δt_{leo} are the receiver's and LEO satellite's clock biases, respectively; λ is the wavelength of the carrier signal transmitted by the LEO satellite; N is the initial carrier phase ambiguity associated with the LEO satellite carrier phase measurement; δt_{iono} and δt_{tropo} are the ionospheric and tropospheric delays, respectively; and v is the measurement noise, which is modeled as a zero-mean white Gaussian random sequence with variance σ_{ϕ}^{2}.

Assuming that no cycle slip occurs when the receiver tracks the carrier phase (i.e., the carrier phase ambiguity remains constant), the difference between the receiver and LEO satellite clock biases and the carrier phase ambiguity are lumped into a single term $c\Delta\delta t(k)$, simplifying (12) to

$$z(k) \triangleq \|\boldsymbol{r}_{\text{r}}(k) - \boldsymbol{r}_{\text{leo}}(k')\|_{2} + c\Delta\delta t(k) + c\delta t_{\text{tropo}}(k) + c\delta t_{\text{iono}}(k) + v(k)$$

$$c\Delta\delta t(k) \triangleq c[\delta t_{\text{r}}(k) - \delta t_{\text{leo}}(k')] + \lambda N. \tag{13}$$

In what follows, the effect of TOF on the LEO satellite's position will be considered negligible, i.e., $\boldsymbol{r}_{\text{leo}}(k') \approx \boldsymbol{r}_{\text{leo}}(k)$. In addition, the LEO satellite's clock bias will be assumed to be constant during the TOF duration, i.e., $\delta t_{\text{leo}}(k') \approx \delta t_{\text{leo}}(k)$. With the latter assumption, the dynamics of $c\Delta\delta t$ can be readily deduced from (5).

LEO-NNPON FRAMEWORK: TRACKING, PREDICTION, AND NAVIGATION

This section describes the three stages of the proposed LEO-NNPON framework for the problem discussed in the "Problem Description" section:

i) *First pass:* EKF-based LEO satellite closed-loop ephemeris tracking;

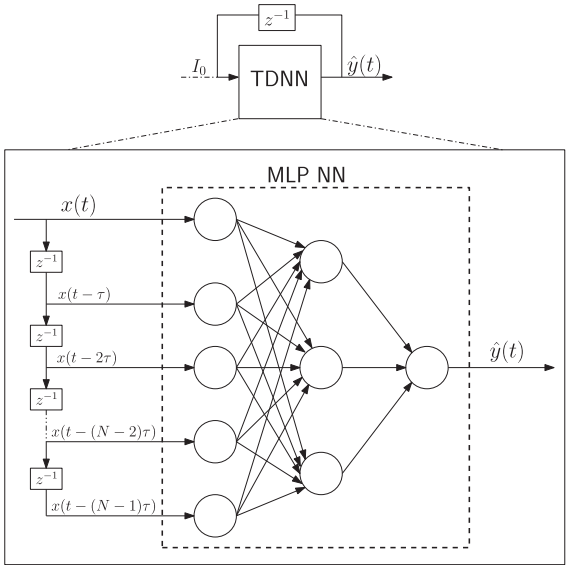

Figure 2.
RNN with TDNN architecture.

ii) *Satellite not in view:* NN-based LEO satellite ephemeris prediction;

iii) *Second pass:* tightly coupled LEO-IMU-based navigation.

EKF-BASED LEO SATELLITE TRACKING

During the LEO satellite's first pass, an EKF is utilized to estimate the LEO satellite's ephemeris. The ground-based tracker with knowledge of its own position $\boldsymbol{r}_{\mathrm{r}}$ extracts carrier phase measurements, modeled in (12), from the LEO satellite's downlink signals. The EKF state vector is given by

$$\boldsymbol{x}_{\mathrm{leo}} = \left[\boldsymbol{r}_{\mathrm{leo}}^{\mathsf{T}}, \dot{\boldsymbol{r}}_{\mathrm{leo}}^{\mathsf{T}}, \Delta\boldsymbol{x}_{\mathrm{clk}}^{\mathsf{T}}\right]^{\mathsf{T}}.$$

The EKF is initialized with LEO ephemeris that got propagated via SGP4 up until the instant the tracker starts producing carrier phase measurements from the LEO downlink signals. The SGP4 propagator can be readily initialized with TLE files. The EKF time update and measurement update can be readily achieved from (1) and (5) and from (12), respectively.

ML-BASED ORBIT PREDICTION

After the LEO's first pass, a refined (tracked) ephemeris is obtained from the EKF. This ephemeris is used to train an NN, whose design is discussed next.

DATA PREPARATION

Since the target outputs (true satellite ephemeris) are not available for training, the satellite's tracked ephemeris from the previous stage is used as the target output. To this end, the tracked ephemeris is preprocessed for use in training the ML model as follows. The final LEO satellite position and velocity state estimate obtained from the EKF is considered to be the best estimate. The short-term accuracy of the two body with the J_2 model is utilized for smoothing the tracked ephemeris [cf., (1)] by backpropagating the final state estimate over the tracking period, which yields a smoother training dataset and more training data points. The features selected as input candidates for the NN are the satellite's 3D position $\boldsymbol{r}_{\mathrm{leo}}$ and velocity $\dot{\boldsymbol{r}}_{\mathrm{leo}}$. The chosen coordinate reference frame is the ECI frame since this eliminates the time-varying effect of Earth's rotation in the ECEF frame.

ARCHITECTURE

Predicting a satellite's ephemeris can be seen as a time-series prediction problem. The NARX architecture has been shown to be highly capable of learning long-term dependencies [48] and predicting time series [49], [50], [51], even chaotic time series [52]. The NARX employs a TDNN (depicted in Figure 2), which is based on a multilayer perceptron feed-forward NN, which simply propagates from input to output in one direction. The time delay aspect is the NN's outputs being fed back as delayed inputs. The NARX takes TLE-initialized, SGP4-propagated position states as inputs. It also has a feedback loop where its output, the estimated ephemeris state values, are fed back as an additional input, as depicted in Figure 3.

OPTIMIZATION AND HYPERPARAMETER TUNING

Next, hyperparameters were chosen to best fit the learned model. Choosing the dimensions of the NN, such as how wide or how deep it is, will greatly affect its performance and ability to generalize, not memorize. Furthermore, since the dynamics of the error between SGP4-propagated ephemeris (initialized from TLE) and true satellite ephemeris are unknown and appear to be nonlinear, multiple activation functions must be investigated, including oscillatory functions (e.g., Snake function). To select the optimal set of hyperparameters, tuners were employed to look within a particular search space. Table 1 summarizes the search space to which the NNs were tuned. These hyperparameters were tuned via Bayesian optimization and

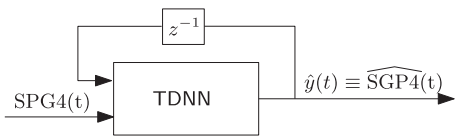

Figure 3.
NARX architecture.

Table 1.

Hyperparameter Search Space	
Parameter	**Value**
Activation function	Linear, ReLU, Tanh, Sigmoid, Snake [53]
Number of layers	[1, 10]
Nodes per layer	[4,512]
Prediction length	[0.1, 240] s
Optimizer	Adam [54], Adagrad [55], SGD, Yogi [56]

compared with hyperparameters selected by a HyperBand optimizer. In addition, the number of time-delayed inputs was varied along with which states were fed into the NN. Finally, optimization was performed to incrementally decrease the learning rate as training loss decreases, and early stopping was implemented to avoid overfitting.

RESULTS

The tuner's conclusions were: two hidden recurrent neural network (RNN) layers with two dense layers, Yogi optimizer, and the number of nodes per layer was 10, with no noticeable improvement in performance when using a higher number of nodes. The prediction length was 400 time delays, where the time interval between delays was 0.01 s. After tuning the NN and comparing different possible combinations of hyperparameters, it was concluded that a wide NN is capable of modeling TLE-SGP4 ephemeris error, and any added layers in depth for introducing higher levels of abstraction are unnecessary. Moreover, increasing the number of delayed inputs degrades the performance as the dimensionality of the input increases without adding much information to the model. An important observation to note is that increasing the number of estimated states results in worse estimated ephemeris. This could be attributed to the limited size of data trained and validated on as well as the incrementally increasing levels of accuracy and abstraction required from the NN as more states are added.

OPPORTUNISTIC NAVIGATION WITH CLOSED-LOOP TRAINED NN LEO EPHEMERIS

During the LEO satellite's second pass, a navigator uses $L \in \mathbb{N}$ LEO satellites to navigate. This is achieved by fusing the navigation observables extracted from the LEO downlink signals with IMU data in a tightly coupled fashion via an EKF. The LEO ephemerides is obtained from the NN. The EKF state vector is given by

$$\boldsymbol{x} = \left[{}^{b}_{g}\bar{\boldsymbol{q}}^{\mathsf{T}},\, \boldsymbol{r}_{\mathrm{r}}^{\mathsf{T}},\, \dot{\boldsymbol{r}}_{\mathrm{r}}^{\mathsf{T}},\, \boldsymbol{b}_{\mathrm{g}}^{\mathsf{T}},\, \boldsymbol{b}_{\mathrm{a}}^{\mathsf{T}},\, \Delta\boldsymbol{x}_{\mathrm{clk},1}^{\mathsf{T}},\, \ldots,\, \Delta\boldsymbol{x}_{\mathrm{clk},L}^{\mathsf{T}} \right]^{\mathsf{T}}$$

where ${}^{b}_{g}\bar{\boldsymbol{q}} \triangleq [{}^{b}_{g}\boldsymbol{q}^{\mathsf{T}},\, {}^{b}_{g}q]^{\mathsf{T}}$ is a 4D unit quaternion representing the orientation of $\{b\}$ fixed at the IMU with respect to $\{g\}$, $\boldsymbol{r}_{\mathrm{r}}$ and $\dot{\boldsymbol{r}}_{\mathrm{r}}$ are the 3D position and velocity of the navigator expressed in $\{g\}$, and $\boldsymbol{b}_{\mathrm{g}}$ and $\boldsymbol{b}_{\mathrm{a}}$ are 3D biases of the IMU's gyroscopes and accelerometers, respectively, expressed in $\{b\}$. Quaternions were chosen to represent the orientation of the navigator with respect to $\{g\}$, since they offer minimal attitude representation without suffering from the singularity of other mathematical attitude representations (e.g., Euler angles). However, since the 4D quaternion is an overdetermined representation of attitude, the estimation error covariance associated with orientation is represented by a three-by-three matrix corresponding to a three-axis error angle vector to prevent degeneracy. The vector $\{\Delta\boldsymbol{x}_{\mathrm{clk},l}\}_{l=1}^{L}$ corresponds to clock error state vector between the receiver and lth LEO satellite [cf., (5)].

The EKF prediction step produces an estimate $\hat{\boldsymbol{x}}(k|j) \triangleq \mathbb{E}[\boldsymbol{x}(k)|\boldsymbol{Z}^{j}]$ of $\boldsymbol{x}(k)$, and an associated estimation error covariance $\mathbf{P}_{\boldsymbol{x}}(k|j)$, where $\mathbb{E}[\cdot|\cdot]$ denotes the conditional expectation, $\boldsymbol{Z}^{j} \triangleq \{\boldsymbol{z}(i)\}_{i=1}^{j}$ is the set of measurements available up to and including time index j, and $k > j$. The IMU measurements (8) and (9) are processed through a vector-valued function of strapdown INS equations in $\{g\}$ that discretize (6) and (7) to obtain [57], [58]

$$\hat{\boldsymbol{x}}_{\mathrm{r}}(k+1|j) = \boldsymbol{f}_{\mathrm{ins}}^{\{g\}}[\hat{\boldsymbol{x}}_{\mathrm{r}}(k|j), \boldsymbol{\omega}_{\mathrm{imu}}(k), \boldsymbol{a}_{\mathrm{imu}}(k)],$$

where the gyroscope and accelerometer bias predictions $\hat{\boldsymbol{b}}_{\mathrm{g}}(k+1|j)$ and $\hat{\boldsymbol{b}}_{\mathrm{a}}(k+1|j)$ follow from (10) and (11), respectively. The INS mechanization equations are performed with the ECI frame as $\{g\}$ since the LEO satellites' position and velocity states are also expressed in ECI. This facilitates the EKF update step as the receiver's and LEO satellites' position and velocity states, and the corresponding estimation error covariances are all expressed in the same reference frame in this case. The ECI strapdown mechanization equations and their linearization to propagate the estimation error covariance. The prediction of the differenced clock states between the receiver and the LEO satellite transmitter follow from (5). The prediction of the LEO satellites' position and velocity is obtained from the NN.

The measurement vector $\boldsymbol{z}$ processed by the EKF update step is defined by stacking all the extracted LEO carrier phase measurements discussed in the "Measurement Model" section. The EKF update step produces an estimate $\hat{\boldsymbol{x}}(k|k)$ and an associated posterior estimation error covariance $\mathbf{P}_{\boldsymbol{x}}(k|k)$.

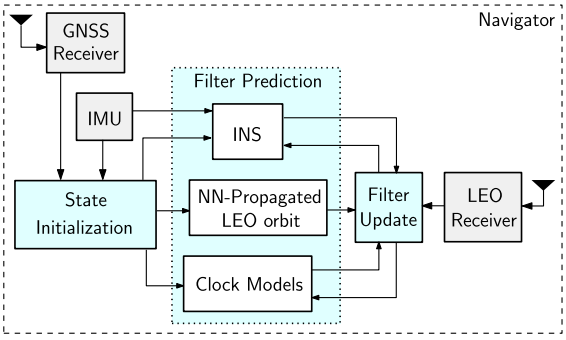

Figure 4.
Tightly coupled LEO-aided INS framework with NN-predicted LEO ephemerides.

Figure 4 summarizes the tightly coupled LEO-aided INS with LEO-NNPON framework with NN-predicted LEO ephemerides. It is worth noting the analogy of this framework to the well-known tightly coupled GNSS-aided INS framework, except for the following: (i) the state is initialized from via the GNSS receiver and IMU, and (ii) the filter prediction stage uses the clock model (5) and the NN-propagated LEO orbit (which was calculated offline after the satellites' first pass). The calculations in (ii) are not deemed to be computationally intensive and can be performed in real time.

EXPERIMENTAL RESULTS

This section presents experimental results validating the efficacy of the LEO-NNPON framework developed in the "LEO-NNPON Framework: Tracking, Prediction, and Navigation" section. The experiments utilized two Orbcomm LEO satellites, namely, Orbcomm FM114 and FM113, whose skyplot of the first and second passes are shown in Figure 5(a). Figure 5(b) shows the elevation history of the LEO satellites relative to the ground-based receiver.

EXPERIMENTAL SETUP

During the first pass, the ground-based stationary tracker utilized a very-high frequency (VHF) antenna, which was connected to an Ettus E312 Universal Software Radio Peripheral (USRP) to receive Orbcomm downlink signals at 137–138 MHz and sample them at 2.4 MSps. The USRP's oscillator was driven by an external, freely running CD-2290 OctoClock. The Multichannel Adaptive TRansceiver Information eXtractor (MATRIX) software-defined receiver (SDR) [16] extracted carrier phase measurements, which were used to track the Orbcomm LEO satellites, as discussed in the "EKF-Based LEO Satellite Tracking" section.

During the second pass, a ground vehicle was equipped with the following:

i) a VectorNav VN-100 microelectro-mechanical systems (MEMS) industrial-grade IMU;

ii) a VHF antenna, connected to the Ettus E312 USRP, which was driven by the freely running CDA-2990 OctoClock;

iii) a Septentrio AsteRx-i V integrated GNSS-INS system and an altimeter, from which the vehicle's ground truth position and velocity were derived.

The collected data during the vehicle's trajectory were stored for offline processing via the MATRIX SDR, which extracted carrier phase measurements from the Obrcomm LEO satellites. These measurements were fused in the tightly coupled LEO-aided INS EKF to estimate the

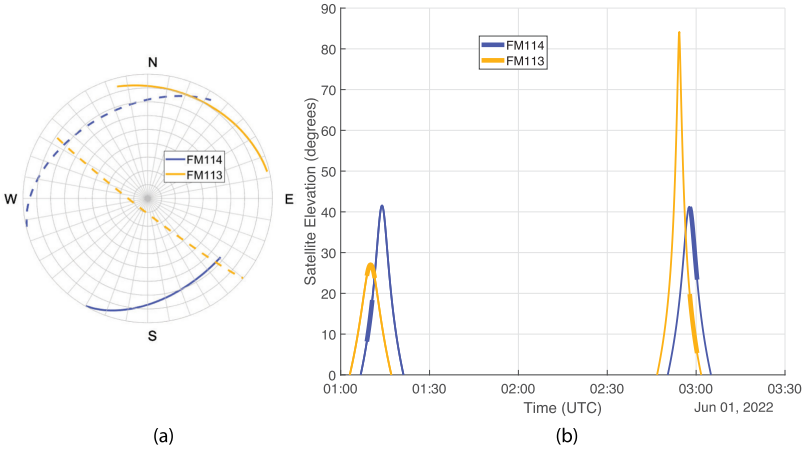

Figure 5.
(a) Skyplot and (b) elevation history of the two Orbcomm LEO satellites' trajectories during their first (solid) and second (dashed) passes. The thick lines indicate the tracking and navigation windows.

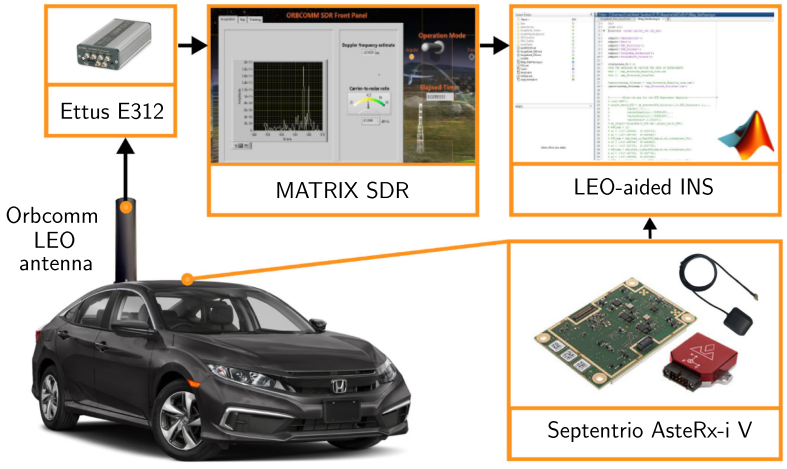

Figure 6.
Experimental hardware and software setup.

vehicle's trajectory, as discussed in the "Opportunistic Navigation with Closed-Loop Trained NN LEO Ephemeris" section.

The hardware and software setup used in the experiment are illustrated in Figure 6.

LEO TRACKING RESULTS

The ground-based stationary tracker's position was obtained from a GNSS receiver. The LEO satellites' position and velocity estimates were initialized from the SGP4-propagated ephemerides of the most recent TLE files available for Orbcomm FM114 and FM113. The associated initial position and velocity estimation error covariances were set to be consistent with the SGP4-propagated TLE ephemerides errors as

$$\begin{aligned}\mathbf{P}_{i_{\mathbf{r}_{\text{leo}}\dot{\mathbf{r}}_{\text{leo}}}}(0|0) &= \text{diag}[\mathbf{P}_{i_{\mathbf{r}_{\text{leo}}}}(0|0), \mathbf{P}_{i_{\dot{\mathbf{r}}_{\text{leo}}}}(0|0)]\\ \mathbf{P}_{i_{\mathbf{r}_{\text{leo}}}}(0|0) &= \mathbf{R}_b^i(0)\mathbf{P}_{b_{\mathbf{r}_{\text{leo}}}}(0|0)[\mathbf{R}_b^i(0)]^{\mathsf{T}}\\ \mathbf{P}_{i_{\dot{\mathbf{r}}_{\text{leo}}}}(0|0) &= \mathbf{R}_b^i(0)\mathbf{P}_{b_{\dot{\mathbf{r}}_{\text{leo}}}}(0|0)[\mathbf{R}_b^i(0)]^{\mathsf{T}}\end{aligned}$$

where $\mathbf{R}_b^i(0)$ is the initial rotation matrix from the LEO satellite's body frame $\{b\}$ to the ECI frame $\{i\}$, and $\mathbf{P}_{b_{\mathbf{r}_{\text{leo}}}}(0|0) = \text{diag}[10^7, 10^4, 10^4]$ m^2 and $\mathbf{P}_{b_{\dot{\mathbf{r}}_{\text{leo}}}}(0|0) = \text{diag}[10^{-2}, 10^{-1}, 10]$ (m/s)^2 are the initial LEO satellite's position and velocity estimation error covariances in the satellite's body frame, respectively. The process noise covariance of the satellite's position and velocity states was determined empirically by evaluating the propagation errors of the adopted two body with J_2 dynamics model with respect to an HPOP [40] in the satellite's body frame, and was rotated to the ECI frame at each time-step of the EKF to propagate the estimation error covariance of the satellite's position and velocity state. The process noise covariance of the clock states was set to be equivalent to a combination of a typical-quality temperature-compensated crystal oscillator (TCXO) and high-quality oven-controlled crystal oscillators (OCXO) pair, whose power-law coefficients are given in Table 2. To find the carrier phase measurement noise variances, the values were manually tuned within a search space in accordance with the innovations calculated for both LEO satellites. The variances were found to be 4 and 10 m^2 for Orbcomm FM114 and FM113, respectively.

Figure 7 shows the position and velocity EKF error plots and associated $\pm 3\sigma$ bounds as well as the open-loop SGP4-propagated ephemeris errors in the satellite's body frame for Orbcomm FM114, respectively. Here, the satellite's downlink signals, which include the satellite's true ephemeris generated by on-board GPS receivers, were decoded for use as ground truth, from which the errors were corrected. The ionospheric and tropospheric delays were corrected in the carrier phase measurements using standard models [47], [59]. Note that closed-loop tracking mainly reduced the position error in the along-track direction, which is typically where most of the open-loop SGP4 propagated error is concentrated [9], [60].

Figure 8 shows the position and velocity EKF error plots and associated $\pm 3\sigma$ bounds as well as the open-loop SGP4-propagated ephemeris errors in the satellite's body frame for Orbcomm FM113, respectively. Similar to

Table 2.

Experimental Oscillator Parameters	
Quality	**Coefficients $\{h_0, h_{-2}\}$**
Typical-quality TCXO	$\{9.4 \times 10^{-20}, 3.8 \times 10^{-21}\}$
High-quality OCXO	$\{2.6 \times 10^{-22}, 4.0 \times 10^{-26}\}$

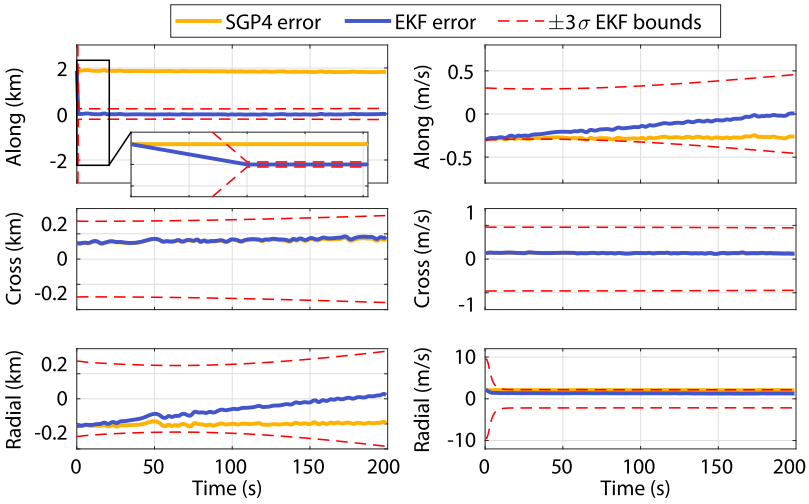

Figure 7.
EKF-tracked position and velocity errors with associated $\pm 3\sigma$ bounds versus open-loop SGP4 errors for Orbcomm FM114 satellite.

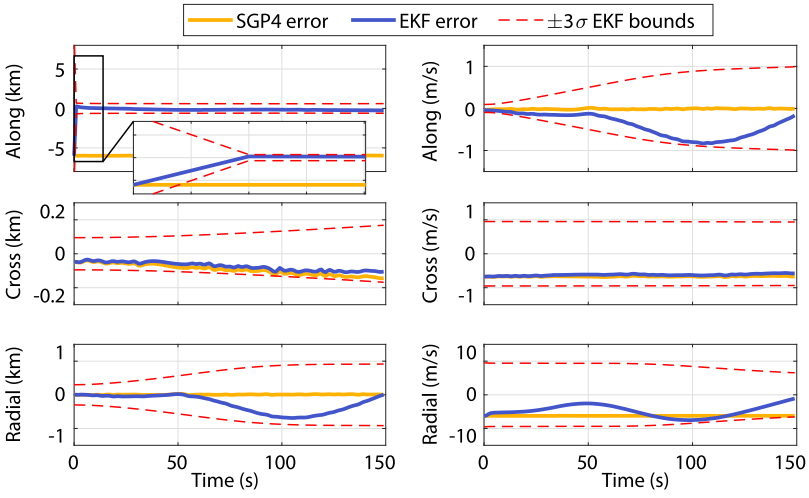

Figure 8.
EKF-tracked position and velocity errors with associated $\pm 3\sigma$ bounds versus open-loop SGP4 errors for Orbcomm FM113 satellite.

Figure 7, note that closed-loop tracking mainly reduced the position error in the along-track direction.

Figure 9 shows the 3D position error magnitude for the EKF-tracked and open-loop SGP4-propagated ephemeris for the two LEO satellites. The position errors resulting from SGP4 propagation of the most recently available TLE files were over 1.8 and 5.9 km for FM114 and FM113, respectively, which were reduced by closed-loop EKF tracking to 199 and 279 m in 200 and 150 s, respectively. The satellite tracking results are summarized in Table 3.

The tracked ephemerides from this first pass is now ready to be used to train the NN, as described in the "Data Preparation" section. Next, the NN is used to predict the satellites' ephemerides. Note that this prediction is implemented while the satellite is not in view, i.e., during the LEO satellite's orbital period in between the first and second passes. As such, there is no additional processing time required by the LEO-NNPON framework during the vehicle navigation stage compared with the open-loop SGP4 framework. Upon the LEO satellites' return to view in the second pass, the satellites' signals are used to navigate the ground vehicle, while using the NN-predicted ephemerides in the LEO-aided INS framework, as described in the "Opportunistic Navigation with Closed-Loop Trained NN LEO Ephemeris" section. The next section shows the ground vehicle navigation results while using the NN-predicted ephemerides versus the SGP-predicted ephemerides.

GROUND VEHICLE NAVIGATION RESULTS

This section presents ground vehicle navigation results during the second passing of the same two Orbcomm LEO

Table 3.

Experimental Results: EKF-Tracked Position Error Magnitude versus Open-Loop SGP4 Errors for the Orbcomm LEO Satellites				
	FM114		FM113	
	SGP4	Tracked	SGP4	Tracked
Position RMSE (m)	1,869	278	5,984	637
Final Error (m)	1,837	199	5,982	279

satellites. The vehicle was driven on the CA-22 freeway next to Irvine, California, USA, for 4.05 km in a duration of 140 s, during which the following was collected:

i) GNSS-INS position and velocity navigation solution, produced by Septentrio AsteRx-i V, which is used as the ground truth to compare against;

ii) data from the VectorNav VN-100 MEMS IMU;

iii) downlink signal samples from Orbcomm FM114 and FM113, which were processed offline via the MATRIX SDR to produce carrier phase measurements.

The carrier phase measurements were fused with the IMU measurements in a tightly coupled fashion via the EKF-based LEO-aided INS, which was initialized with the GNSS-INS position and velocity solution.

Three vehicle navigation frameworks, all initialized with the GNSS-INS position and velocity solution, are compared: (i) unaided INS, (ii) LEO-aided INS, which uses SGP4-propagated LEO ephemerides, and (iii) LEO-aided INS with LEO-NNPON. Figures 10 and 11 show the position and velocity EKF error plots and associated $\pm 3\sigma$ bounds for each framework.

The clock error state estimates were initialized as follows. The clock bias term was initialized by subtracting the initial estimated range from the initial carrier phase measurement. The clock drift term was initialized by subtracting the initial time rate of change of the estimated range from the initial time rate of change of the carrier phase measurement, such that

$$\Delta\hat{\delta}t_{\mathrm{r,leo},l}(0|0) = \phi_l(0) - \hat{d}_l(0)$$
$$\Delta\hat{\dot{\delta}}t_{\mathrm{r,leo},l}(0|0) = \frac{1}{T}[\phi_l(1) - \phi_l(0)] - \frac{1}{T}\left[\hat{d}_l(1) - \hat{d}_l(0)\right]$$

where $\phi_l(0)$ and $\phi_l(1)$ are the first two carrier phase measurements from the lth LEO satellite, T is the sampling period, and $\hat{d}_l(j) = \|\hat{\boldsymbol{r}}_{\mathrm{r}}(j) - \boldsymbol{r}_{\mathrm{leo},l}(j)\|$ for $j = 0, 1$. Note that in the above clock state initialization equations, the satellite's position vector is taken from the SGP4 and the NN ephemeris sets, respectively, for each LEO-aided INS navigation solution [i.e., frameworks (ii) and (iii)].

The process noise covariance of the clock error states was set to be equivalent to a combination of a typical-quality TCXO and high-quality OCXO pair, whose power-law coefficients are given in Table 2. The ground vehicle's state estimation error covariance was initialized as

$$\begin{aligned}\mathbf{P}_{\boldsymbol{x}}(0|0) &= \mathrm{diag}[\mathbf{P}_{\boldsymbol{q}\boldsymbol{r}_{\mathrm{r}}\dot{\boldsymbol{r}}_{\mathrm{r}}}(0|0), \mathbf{P}_{\boldsymbol{b}_{\mathrm{imu}}}(0|0), \mathbf{P}_{\mathrm{clk},1}(0|0),\\ &\qquad \mathbf{P}_{\mathrm{clk},2}(0|0)]\\ \mathbf{P}_{\boldsymbol{q}\boldsymbol{r}_{\mathrm{r}}\dot{\boldsymbol{r}}_{\mathrm{r}}}(0|0) &= [10^{-2} \times \mathbf{I}_{3\times 3}, 10 \times \mathbf{I}_{3\times 3}, \mathbf{I}_{3\times 3}]\\ \mathbf{P}_{\boldsymbol{b}_{\mathrm{imu}}}(0|0) &= [10^{-4} \times \mathbf{I}_{3\times 3}, 10^{-4} \times \mathbf{I}_{3\times 3}]\\ \mathbf{P}_{\mathrm{clk},i}(0|0) &= [10, 10^{-2}], \quad i = 1, 2\end{aligned}$$

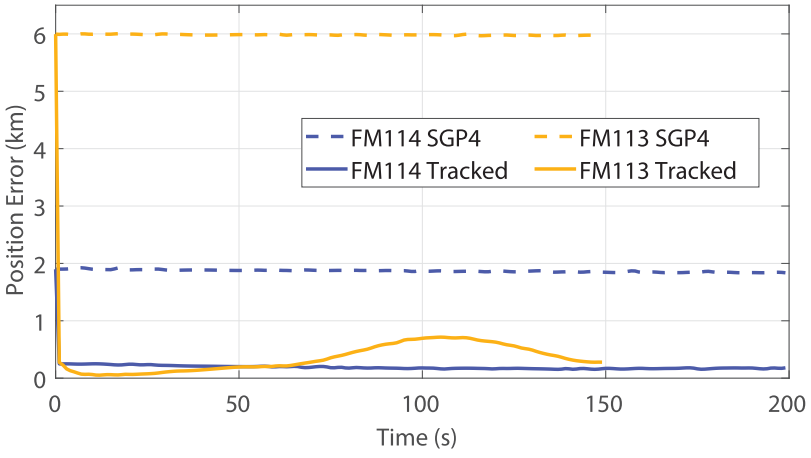

Figure 9.
EKF-tracked position error magnitude versus open-loop SGP4 errors for Orbcomm FM114 and FM113.

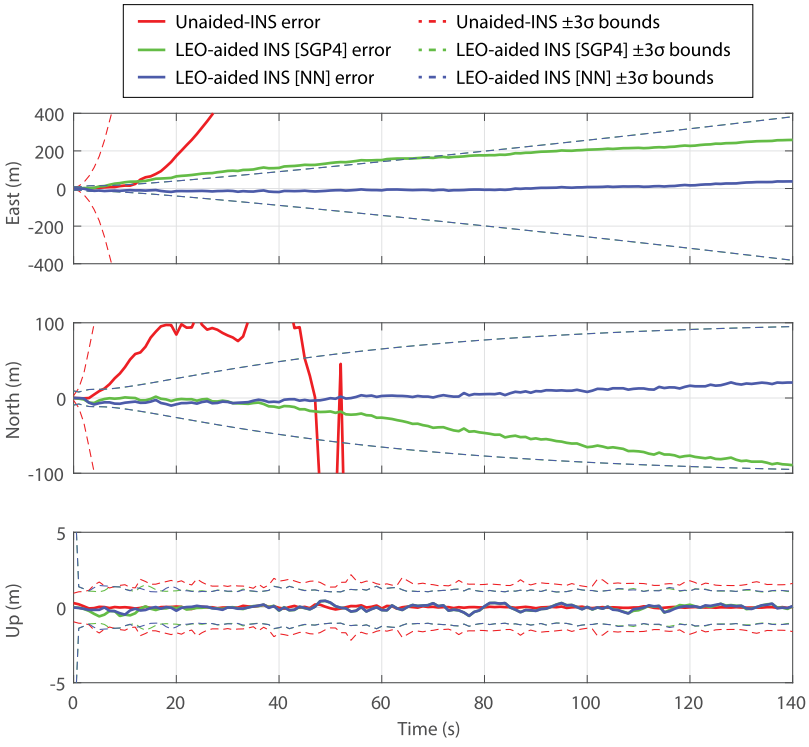

Figure 10.
EKF ground vehicle position errors and associated $\pm 3\sigma$ bounds in the ENU frame for (i) unaided INS, (ii) LEO-aided INS with SGP4-propagated ephemerides, and (iii) LEO-aided INS with NN-predicted ephemerides.

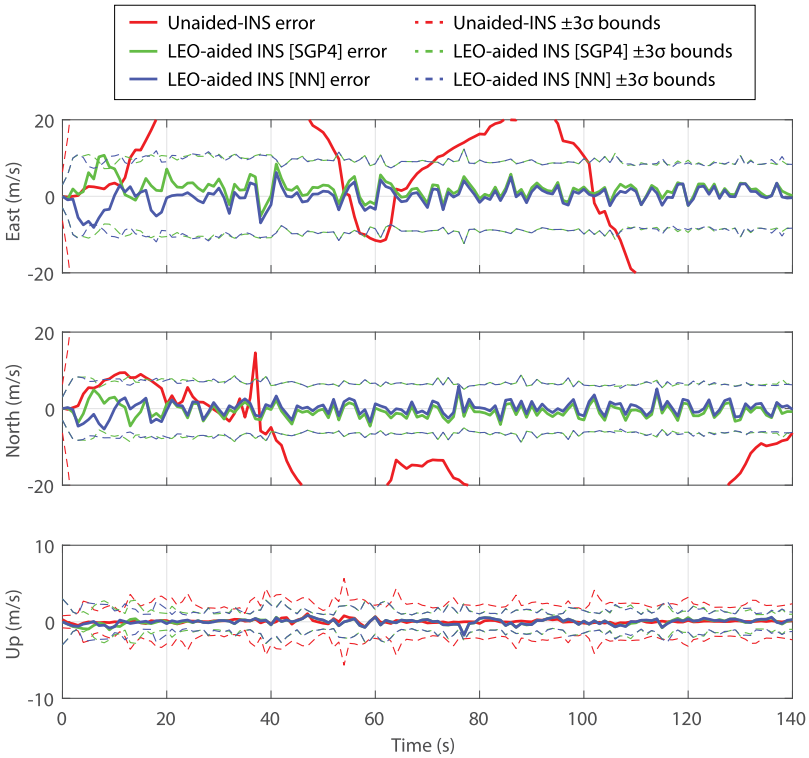

Figure 11.
EKF ground vehicle velocity errors and associated $\pm 3\sigma$ bounds in the ENU frame for (i) unaided INS, (ii) LEO-aided INS with SGP4-propagated ephemerides, and (iii) LEO-aided INS with NN-predicted ephemerides.

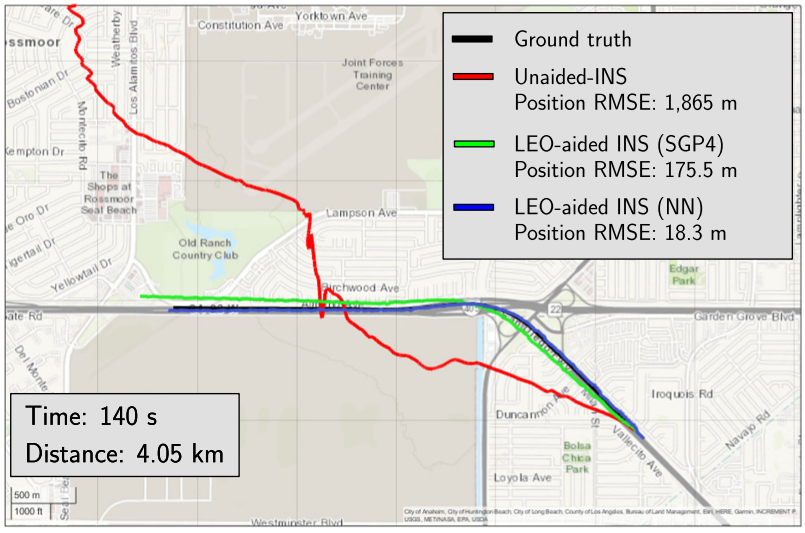

Figure 12.
Experimental results showing the ground vehicle's ground truth trajectory (traveling right to left) and estimated trajectory with: (i) unaided INS, (ii) LEO-aided INS with SGP4-propagated ephemerides, and (iii) LEO-aided INS with NN-predicted ephemerides.

where $\mathbf{P}_{\boldsymbol{q}_{\mathrm{r}}\boldsymbol{r}_{\mathrm{r}}\dot{\boldsymbol{r}}_{\mathrm{r}}}(0|0)$ is the initial ground vehicle orientation, position, and velocity covariance with units of $[\mathrm{rad}^2, \mathrm{m}^2, (\mathrm{m/s})^2]$ and $\mathbf{P}_{\boldsymbol{b}_{\mathrm{imu}}}(0|0)$ is the initial IMU gyroscope and accelerometer biases covariance with units of $[(\mathrm{rad/s})^2, (\mathrm{m/s2})^2]$. To find the carrier phase measurement noise variances, the values were manually tuned in a search space in accordance with the innovations calculated for both LEO satellites. The variances were found to be 1 and 2 m^2 for Orbcomm FM114 and FM113, respectively.

The following can be concluded from Figures 10 and 11. First, as expected, the EKF position and velocity error of the unaided INS immediately diverge (due to the absence of GNSS aiding) in the East and North direction, while the error and uncertainty remains bounded in the up direction due to altimeter measurements. Second, the $\pm 3\sigma$ bounds of the vehicle's position and velocity states are equal whether SGP4 or the NN ephemerides are used; however, the error divergence with the NN is much lower than that with SGP4. Hence, the NN predicted ephemerides is closer to the LEO satellite's true ephemerides than that of SGP4. The vehicle's navigation solution from each framework are shown in Figure 12 and summarized in Table 4.

CONCLUSION

This article developed the LEO-NNPON framework. The framework is composed of the following three stages:

i) tracking the LEO satellites during the first pass;

ii) predicting the LEO satellites' ephemerides when the satellite is not in view, by utilizing the NN, which was trained on the tracked ephemerides;

iii) navigating with LEO satellites by aiding the navigator-mounted IMU with navigation observables extracted from downlink LEO satellites, while utilizing the NN-predicted LEO ephemerides.

The efficacy of the improved LEO predicted ephemerides was demonstrated experimentally by showing improved ground vehicle navigation with signals from two Orbcomm LEO satellites, while using the NN-predicted compared to the SGP4 propagator. It was shown that over a 4.05 km, the LEO-aided INS with SGP4 achieved a 3D position RMSE of 175.5 m, whereas the LEO-aided INS with NN achieved a position RMSE of 18.3 m. It is worth highlighting that while this article demonstrated the application of the LEO-NNPON framework on Orbcomm satellites, LEO-NNPON can be applied to other LEO constellations (e.g., Starlink and OneWeb). Future research could analyze the performance as a function of the tracking duration, leading to the minimum duration required of the tracked pass.

Table 4

Experimental Results: Comparison of Different Navigation Frameworks			
	Unaided INS	**LEO-INS [SGP4]**	**LEO-INS [NN]**
Position RMSE (m)	1,865	175.5	18.3
Final error (m)	2,841	273.4	43.0

ACKNOWLEDGMENTS

This work was supported in part by the Air Force Office of Scientific Research (AFOSR) under Grant FA9550-22-1-0476 and in part by the National Science Foundation (NSF) under Grant 2240512. The authors would like to thank Dr. Erik Blasch for the extensive insightful discussions and Sharbel Kozhaya and Nadim Khairallah for their help with data collection and processing.

REFERENCES

[1] B. Evans, P. Thompson, G. Corazza, A. Vanelli-Coralli, and E. Candreva, "1945–2010: 65 years of satellite history from early visions to latest missions," *Proc. IEEE*, vol. 99, no. 11, pp. 1840–1857, Nov. 2011, doi: 10.1109/jproc.2011.2159467.

[2] S. Marcuccio, S. Ullo, M. Carminati, and O. Kanoun, "Smaller satellites, larger constellations: Trends and design issues for Earth observation systems," *IEEE Aerosp. Electron. Syst. Mag.*, vol. 34, no. 10, pp. 50–59, Oct. 2019, doi: 10.1109/maes.2019.2928612.

[3] K. Li, C. Hofmann, H. Reder, and A. Knopp, "A techno-economic assessment and tradespace exploration of low Earth orbit mega-constellations," *IEEE Commun. Mag.*, vol. 61, no. 2, pp. 24–30, Feb. 2023, doi: 10.1109/mcom.001.2200312.

[4] Y. Liao, S. Li, X. Hong, J. Shi, and L. Cheng, "Integration of communication and navigation technologies toward LEO-enabled 6G networks: A survey," *Space: Sci. Technol.*, vol. 3, pp. 1–19, Oct. 2023, doi: 10.34133/space.0092.

[5] R. Blazquez-Garcia, D. Cristallini, M. Ummenhofer, V. Seidel, J. Heckenbach, and D. O'Hagan, "Capabilities and challenges of passive radar systems based on broadband low-Earth orbit communication satellites," *IET Radar, Sonar Navigation*, vol. 18, no. 1, pp. 78–92, 2024, doi: 10.1049/rsn2.12446.

[6] H. Dureppagari, C. Saha, H. Dhillon, and R. Buehrer, "NTN-based 6G localization: Vision, role of LEOs, and open problems," *IEEE Wireless Commun.*, vol. 30, no. 6, pp. 44–51, Dec. 2023, doi: 10.1109/mwc.007.2300224.

[7] L. Ries et al.,, "LEO-PNT for augmenting Europe's space-based PNT capabilities," in *Proc. IEEE/ION Position, Location, Navigation Symp.*, Apr. 2023, pp. 329–337, doi: 10.1109/plans53410.2023.10139999.

[8] E. Blasch, D. Shen, G. Chen, C. Sheaff, and K. Pham, "Space object tracking uncertainty analysis with the URREF ontology," in *Proc. IEEE Aerosp. Conf.*, Mar. 2021, pp. 1–9, doi: 10.1109/aero50100.2021.9438207.

[9] N. Khairallah and Z. Kassas, "Ephemeris tracking and error propagation analysis of LEO satellites with application to opportunistic navigation," *IEEE Trans. Aerosp. Electron. Syst.*, vol. 60, no. 2, pp. 1242–1259, Apr. 2024, doi: 10.1109/taes.2023.3325797.

[10] Z. Kassas, N. Khairallah, and S. Kozhaya, "Ad Astra: Simultaneous tracking and navigation with mega-constellation LEO satellites," *IEEE Aerosp. Electron. Syst. Mag.*, vol. 39, no. 9, pp. 46–71, Sep. 2024, doi: 10.1109/MAES.2023.3267440.

[11] F. Farhangian and R. Landry, "Multi-constellation software-defined receiver for Doppler positioning with LEO satellites," *Sensors*, vol. 20, no. 20, pp. 5866–5883, Oct. 2020, doi: 10.3390/s20205866.

[12] M. Orabi, J. Khalife, and Z. Kassas, "Opportunistic navigation with Doppler measurements from iridium NEXT and Orbcomm LEO satellites," in *Proc. IEEE Aerosp. Conf.*, Mar. 2021, pp. 1–9, doi: 10.1109/aero50100.2021.9438454.

[13] C. Huang, H. Qin, C. Zhao, and H. Liang, "Phase - time method: Accurate Doppler measurement for Iridium NEXT signals," *IEEE Trans. Aerosp. Electron. Syst.*, vol. 58, no. 6, pp. 5954–5962, Dec. 2022, doi: 10.1186/s13634-023-01022-1.

[14] C. Pinell, F. Prol, M. Bhuiyan, and J. Praks, "Receiver architectures for positioning with low Earth orbit satellite signals: A survey," *EURASIP J. Adv. Signal Process.*, vol. 2023, pp. 60–80, 2023, doi: 10.1186/s13634-023-01022-1.

[15] J. Khalife, M. Neinavaie, and Z. Kassas, "The first carrier phase tracking and positioning results with Starlink LEO satellite signals," *IEEE Trans. Aerosp. Electron. Syst.*, vol. 56, no. 2, pp. 1487–1491, Apr. 2022, doi: 10.1109/taes.2021.3113880.

[16] S. Kozhaya and Z. Kassas, "Blind receiver for LEO beacon estimation with application to UAV carrier phase differential navigation," in *Proc. ION GNSS Conf.*, 2022, pp. 2385–2397, doi: 10.33012/2022.18582.

[17] Z. Kassas et al., "Navigation with multi-constellation LEO satellite signals of opportunity: Starlink, Oneweb, Orbcomm, and Iridium," in *Proc. IEEE/ION Position, Location, Navigation Symp.*, Apr. 2023, pp. 338–343, doi: 10.1109/plans53410.2023.10140066.

[18] S. Kozhaya, H. Kanj, and Z. Kassas, "Blind Doppler tracking and positioning with NOAA LEO satellite signals," in *Proc. ION GNSS Conf.*, Sep. 2023, pp. 363–372, doi: 10.33012/2023.19463.

[19] M. Neinavaie and Z. Kassas, "Cognitive sensing and navigation with unknown OFDM signals with application to terrestrial 5G and Starlink LEO satellites," *IEEE J. Sel. Areas Commun.*, vol. 42, no. 1, pp. 146–160, Jan. 2024, doi: 10.1109/jsac.2023.3322811.

[20] N. Khairallah and Z. Kassas, "An interacting multiple model estimator of LEO satellite clocks for improved positioning," in *Proc. IEEE Veh. Technol. Conf.*, 2022, pp. 1–5, doi: 10.1109/vtc2022-spring54318.2022.9860828.

[21] L. Ye, N. Gao, Y. Yang, L. Deng, and H. Li, "Three satellites dynamic switching range integrated navigation and positioning algorithm with clock bias cancellation and altimeter assistance," *Aerospace*, vol. 10, no. 5, pp. 411–438, 2023, doi: 10.3390/aerospace10050411.

[22] A. El-Mowafy, K. Wang, Y. Li, and A. Allahvirdi-Zadeh, "The impact of orbital and clock errors on positioning from LEO constellations and proposed orbital solutions," *Int. Arch. Photogrammetry, Remote Sens. Spatial Inf. Sci.*, vol. 48, pp. 1111–1117, 2023, doi: 10.5194/isprs-archives-xlviii-1-w2-2023-1111-2023.

[23] B. Schutz, B. Tapley, and G. Born, *Statistical Orbit Determination*. New York, NY, USA: Elsevier, 2004, doi: 10.1016/b978-0-12-683630-1.x5019-x.

[24] J. Vetter, "Fifty years of orbit determination: Development of modern astrodynamics methods," *Johns Hopkins APL Tech. Dig.*, vol. 27, no. 3, pp. 239–252, Nov. 2007. [Online]. Available: https://secwww.jhuapl.edu/techdigest/content/techdigest/pdf/V27-N03/27-03-Vetter.pdf

[25] D. Vallado and P. Crawford, "SGP4 orbit determination," in *Proc. AIAA/AAS Astrodynamics Specialist Conf. Exhibit*, Aug. 2008, pp. 6770–6799, doi: 10.2514/6.2008-6770.

[26] North American Aerospace Defense Command (NORAD), "Two-line element sets," Accessed: Aug. 1, 2024. [Online]. Available: http://celestrak.com/NORAD/elements/

[27] X. Tian, G. Chen, E. Blasch, K. Pham, and Y. Bar-Shalom, "Comparison of three approximate kinematic models for space object tracking," in *Proc. Int. Conf. Inf. Fusion*, 2013, pp. 1005–1012. [Online]. Available: https://ieeexplore.ieee.org/abstract/document/6641105.

[28] R. Deng, H. Qin, H. Li, D. Wang, and H. Lv, "Noncooperative LEO satellite orbit determination based on single pass Doppler measurements," *IEEE Trans. Aerosp. Electron. Syst.*, vol. 59, no. 2, pp. 1096–1106, Apr. 2023, doi: 10.1109/taes.2022.3194977.

[29] U. Majumder, E. Blasch, and D. Garren, *Deep Learning for Radar and Communications Automatic Target Recognition*. Norwood, MA, USA: Artech House, 2020.

[30] Y. Wang et al., "Gaussian-binary classification for resident space object maneuver detection," *Acta Astronautica*, vol. 187, pp. 438–446, Oct. 2021, doi: 10.1016/j.actaastro.2021.06.046.

[31] S. Shen, C. Sheaff, M. Guo, E. Blasch, K. Pham, and G. Chen, "Three-dimensional convolutional neural network (3D-CNN) for satellite behavior discovery," in *Proc. SPIE Sensors Syst. Space Appl.*, 2021, vol. 11755, pp. 1–18, doi: 10.1117/12.2589044.

[32] S. Sharma and J. Cutler, "Robust orbit determination and classification: A learning theoretic approach," *IPN Prog. Rep.*, vol. 42, pp. 1–20, 2015, Art. no. 203. [Online]. Available: tmo.jpl.nasa.gov/progress_report/42-203/203D.pdf

[33] F. Feng, Y. Zhang, H. Li, Y. Fang, Q. Huang, and X. Tao, "A novel space-based orbit determination method based on distribution regression and its sparse solution," *IEEE Access*, vol. 7, pp. 133203–133217, 2019, doi: 10.1109/access.2019.2940893.

[34] H. Peng and X. Bai, "Limits of machine learning approach on improving orbit prediction accuracy using support vector machine," in *Proc. Adv. Maui Opt. Space Surveill. Technol. Conf.*, 2017, pp. 1–22, doi: 10.2514/1.i010616.

[35] H. Peng and X. Bai, "Artificial neural network–based machine learning approach to improve orbit prediction accuracy," *J. Spacecraft Rockets*, vol. 55, no. 5, pp. 1248–1260, 2018, doi: 10.2514/1.a34171.

[36] H. Peng and X. Bai, "Comparative evaluation of three machine learning algorithms on improving orbit prediction accuracy," *Astrodynamics*, vol. 3, no. 4, pp. 325–343, 2019, doi: 10.1007/s42064-018-0055-4.

[37] N. Salleh, S. Yuhaniz, N. Azmi, and S. Sabri, "Enhancing simplified general perturbations-4 model for orbit propagation using deep learning: A review," in *Proc. Int. Conf. Softw. Comput. Appl.*, 2019, pp. 27–32, doi: 10.1145/3316615.3316675.

[38] T. Mortlock and Z. Kassas, "Assessing machine learning for LEO satellite orbit determination in simultaneous tracking and navigation," in *Proc. IEEE Aerosp. Conf.*, Mar. 2021, pp. 1–8, doi: 10.1109/aero50100.2021.9438144.

[39] S. Kozhaya, J. Haidar-Ahmad, A. Abdallah, Z. Kassas, and S. Saab, "Comparison of neural network architectures for simultaneous tracking and navigation with LEO satellites," in *Proc. ION GNSS Conf.*, 2021, pp. 2507–2520, doi: 10.33012/2021.18110.

[40] Analytical Graphics, Inc, "Systems Tool Kit (STK)," Apr. 2020. [Online]. Available: https://www.agi.com/getmedia/172b0f02-7469-4fbf-9d5c-9c6e6f36aa87/STK-Pro-Product-Specsheet.pdf?ext=.pdf

[41] J. Haidar-Ahmad, N. Khairallah, and Z. Kassas, "A hybrid analytical-machine learning approach for LEO satellite orbit prediction," in *Proc. Int. Conf. Inf. Fusion*, 2022, pp. 1–7, doi: 10.23919/fusion49751.2022.9841298.

[42] S. Hayek, J. Saroufim, and Z. Kassas, "Ephemeris error modeling in opportunistic LEO satellite tracking with pseudorange and Doppler measurements," in *Proc. ION GNSS Conf.*, Sep. 2023, pp. 2123–2133, doi: 10.33012/2023.19453.

[43] O. Montenbruck and E. Gill, *Satellite Orbits: Models, Methods, and Applications*. Berlin, Germany: Springer, 2000, doi: 10.1115/1.1451162.

[44] J. Morales, J. Khalife, U. Santa Cruz, and Z. Kassas, "Orbit modeling for simultaneous tracking and navigation using LEO satellite signals," in *Proc. ION GNSS Conf.*, Sep. 2019, pp. 2090–2099, doi: 10.33012/2019.17029.

[45] R. Brown and P. Hwang, *Introduction to Random Signals and Applied Kalman Filtering With Matlab Exercises*, 4th ed. Hoboken, NJ, USA: Wiley, 2012.

[46] J. Farrell and M. Barth, *The Global Positioning System and Inertial Navigation*. New York, NY, USA: McGraw-Hill, 1998.

[47] P. Misra and P. Enge, *Global Positioning System: Signals, Measurements, and Performance*, 2nd ed. Dallas, TX, USA: Ganga-Jamuna Press, 2010.

[48] T. Lin, B. Horne, P. Tino, and C. Giles, "Learning long-term dependencies in NARX recurrent neural networks," *IEEE Trans. Neural Netw.*, vol. 7, no. 6, pp. 1329–1338, Nov. 1996, doi: 10.1109/72.548162.

[49] H. Siegelmann, B. Horne, and C. Giles, "Computational capabilities of recurrent NARX neural networks," *IEEE Trans. Systems, Man, Cybern., Part B.*, vol. 27, no. 2, pp. 208–215, Apr. 1997, doi: 10.1109/3477.558801.

[50] J. Menezes, P. Maria, and G. Barreto, "Long-term time series prediction with the NARX network: An empirical evaluation," *Neurocomputing*, vol. 71, no. 16-18, pp. 3335–3343, 2008, doi: 10.1016/j.neucom.2008.01.030.

[51] H. Xie, H. Tang, and Y. Liao, "Time series prediction based on NARX neural networks: An advanced approach," in *Proc. IEEE Int. Conf. Mach. Learn. Cybern.*, 2009, pp. 1275–1279, doi: 10.1109/icmlc.2009.5212326.

[52] E. Diaconescu, "The use of NARX neural networks to predict chaotic time series," *WSEAS Trans. Comput. Res.*, vol. 3, no. 3, pp. 182–191, 2008, doi: 10.5555/1466884.1466892.

[53] L. Ziyin, T. Hartwig, and M. Ueda, "Neural networks fail to learn periodic functions and how to fix it," *Adv. Neural Inf. Process. Syst.*, vol. 33, pp. 1583–1594, 2020, doi: 10.48550/arXiv.2006.08195.

[54] D. Kingma and J. Ba, "Adam: A method for stochastic optimization," in *Proc. Int. Conf. Learn. Representations*, 2015, pp. 1–15, doi: 10.48550/arXiv.1412.6980.

[55] J. Duchi, E. Hazan, and Y. Singer, "Adaptive subgradient methods for online learning and stochastic optimization," *J. Mach. Learn. Res.*, vol. 12, no. 7, pp. 2121–2159, 2011, doi: 10.5555/1953048.2021068.

[56] M. Zaheer, S. Reddi, D. Sachan, S. Kale, and S. Kumar, "Adaptive methods for nonconvex optimization," in *Proc. Int. Conf. Neural Inf. Process. Syst.*, 2018, pp. 9815–9825, doi: 10.5555/3327546.3327647.

[57] P. Groves, *Principles of GNSS, Inertial, and Multisensor Integrated Navigation Systems*, 2nd ed. Norwood, MA, USA: Artech House, 2013.

[58] J. Morales and Z. Kassas, "Tightly-coupled inertial navigation system with signals of opportunity aiding," *IEEE Trans. Aerosp. Electron. Syst.*, vol. 57, no. 3, pp. 1930–1948, Jun. 2021, doi: 10.1109/taes.2021.3054067.

[59] N. Khairallah, "Towards opportunistic navigation with LEO satellites: Adaptive clock estimation and closed-loop ephemeris tracking," Master's thesis, Univ. California, Irvine, CA, USA, 2022. [Online]. Available: https://escholarship.org/uc/item/5q98d5vr

[60] P. Easthope, "Examination of SGP4 along-track errors for initially circular orbits," *IMA J. Appl. Math.*, vol. 80, no. 2, pp. 554–568, 2015, doi: 10.1093/imamat/hxt056.